

SPT-CL J0417–4748: A Deep Chandra Study of a Relaxed Galaxy Cluster Without Central Star Formation

TAWEEWAT SOMBOONPANYAKUL ,^{1,2} ADAM B. MANTZ ,² STEVEN W. ALLEN ,^{2,3,4} ANTHONY M. FLORES ,^{2,3,5}
 R. GLENN MORRIS ,^{2,3,4} HALEY R. STUEBER ,^{2,3} LINDSEY E. BLEEM ,⁶ BENJAMIN FLOYD ,⁷
 JULIE HLAVACEK-LARRONDO ,⁸ AND KEUNHO J. KIM ,⁹

¹Department of Physics, Faculty of Science, Chulalongkorn University, 254 Phayathai Road, Pathumwan, Bangkok 10330, Thailand

²Kavli Institute for Particle Astrophysics and Cosmology, Stanford University, 452 Lomita Mall, Stanford, CA 94305, USA

³Department of Physics, Stanford University, 382 Via Pueblo Mall, Stanford, CA 94305, USA

⁴SLAC National Accelerator Laboratory, 2575 Sand Hill Road, Menlo Park, CA 94025, USA

⁵Department of Physics and Astronomy, Rutgers University 136 Frelinghuysen Rd Piscataway, NJ 08854, USA

⁶High-Energy Physics Division, Argonne National Laboratory, 9700 South Cass Avenue., Lemont, IL, 60439, USA

⁷Institute of Cosmology & Gravitation, University of Portsmouth, Dennis Sciama Building, Portsmouth, PO1 3FX, UK

⁸Département de Physique, Université de Montréal, Succ. Centre-Ville, Montréal, Québec, H3C 3J7, Canada

⁹IPAC, California Institute of Technology, 1200 E. California Boulevard, Pasadena, CA 91125, USA

ABSTRACT

We present an in-depth Chandra X-ray analysis of the galaxy cluster SPT-CL J0417–4748 (hereafter SPT J0417), at $z = 0.58$, with a focus on its thermodynamic properties and the apparent absence of central star formation. Utilizing a total Chandra exposure of 103 ks, we find that the large-scale X-ray morphology is consistent with a dynamically relaxed, cool-core system. The intracluster medium (ICM) shows a central density of $0.08 \pm 0.01 \text{ cm}^{-3}$, a central pseudo-entropy of $26_{-5}^{+6} \text{ keV cm}^2$ and a central cooling time of $515_{-75}^{+96} \text{ Myr}$, values typical of massive cool-core clusters. Despite these conditions, no evidence of recent or ongoing star formation is detected in the brightest cluster galaxy (BCG). Spectral energy distribution (SED) fitting of DES photometry indicates that the bulk of the stellar population formed at $z \sim 1.25$, with no significant star formation over the past ~ 3 Gyr, while optical spectra from Magellan show no [O II] emission. Complementary ASKAP radio and Spitzer infrared data indicate a lack of strong current AGN activity in the BCG. SPT J0417 exemplifies massive, relaxed, cool-core clusters in which cooling and star formation appear almost completely quenched, providing valuable insights into how AGN feedback regulates the long-term thermal balance of the intracluster medium.

Keywords: Galaxy clusters (584)

1. INTRODUCTION

Early X-ray observations of galaxy clusters revealed a hot ($\sim 10^7 \text{ K}$), X-ray-emitting plasma known as the intracluster medium (ICM), permeating the cluster environment (Fabian & Nulsen 1977; White et al. 1991; Edge et al. 1992; Voit 2005). This plasma is the dominant baryonic matter component of galaxy clusters. Some systems, known as "cool-core" clusters, exhibit high and sharply peaked central ICM densities and relatively low temperatures (Allen et al. 2001; McNamara & Nulsen 2007; Werner et al. 2014). In the absence of a heating

mechanism, the gas in cool cores would rapidly cool and flow inward, generating a "cooling flow" (Sarazin 1986; Fabian 1994). This process would deposit large amounts of cold gas onto the bright central galaxy (BCG), fueling significant star formation.

However, observations reveal much lower star formation rates than predicted, a discrepancy referred to as the "cooling flow problem" (O'Dea et al. 2008; Donahue et al. 2015; McDonald et al. 2018). Active galactic nucleus (AGN) feedback, driven by the energetic output of supermassive black holes (SMBHs) residing in cluster cores, is thought to play a central role in regulating radiative cooling by coupling to the surrounding intracluster medium and offsetting excessive energy

losses (Fabian 2012; McNamara & Nulsen 2012). This feedback manifests through radiation, wind, and/or relativistic jets (Rafferty et al. 2006; McNamara & Nulsen 2007; Hlavacek-Larrondo et al. 2013).

Over the past few decades, observations have revealed a wide range of star formation rates (SFRs) in cool-core BCGs, from extreme cases such as the Phoenix Cluster with SFRs of $\sim 800 M_{\odot} \text{ yr}^{-1}$, down to just a few $M_{\odot} \text{ yr}^{-1}$ in systems like Abell 478 and RX J1720.1+2638, and even lower rates ($< 1 M_{\odot} \text{ yr}^{-1}$) in Abell 2029 (Cavagnolo et al. 2009; McDonald et al. 2013; Fraser-Mckelvie et al. 2014; McDonald et al. 2018). These findings have led to several theoretical models exploring the relationships between SFR, ICM cooling, and AGN feedback.

One proposed scenario suggests that some massive cool-core clusters exhibit high SFRs ($> 100 M_{\odot} \text{ yr}^{-1}$) owing to a saturation in AGN feedback heating, particularly in the most massive systems (McDonald et al. 2018; Calzadilla et al. 2022). However, the existence of many massive cool-core clusters with little to no star formation in their BCGs indicates that not all such systems have reached this saturation threshold. This raises important questions regarding the physical conditions under which AGN feedback becomes inefficient at regulating cooling. Identifying more examples of massive cool-core clusters with a broad range of SFRs will provide further insight into the underlying mechanisms governing cooling and feedback, and their role in the broader context of galaxy cluster evolution.

SPT J0417 ($z = 0.58$) represents an intriguing case of a massive, cool-core cluster exhibiting minimal star formation activity in its BCG, indicating that AGN feedback may remain below the saturation threshold. Identified in the 2500 deg² South Pole Telescope-Sunyaev-Zel'dovich (SPT-SZ) cluster survey (Williamson et al. 2011; Bleem et al. 2015), this cluster was observed with the Chandra X-ray Observatory for 22 ks in 2013. McDonald et al. (2013, 2016a) classified this object as a typical cool-core system, with no evidence of star formation in the central galaxy. In this study, we present a deeper observation of SPT J0417 using combined Chandra data totaling 110 ks in exposure time. These observations enable a more detailed exploration of the cluster core and provide an opportunity to investigate the potential mechanisms that could suppress star formation in the cluster's center.

The remainder of this paper is organized as follows. Section 2 outlines the Chandra X-ray observations and data reduction, and presents supporting multiwavelength datasets, including infrared, radio, and optical spectroscopic observations of BCG. The primary X-ray

analysis and results are detailed in Section 3, and a summary of the findings and their broader implications are presented in Section 4. Throughout this work, we adopt $H_0 = 70 \text{ km s}^{-1} \text{Mpc}^{-1}$, $\Omega_m = 0.3$, and $\Omega_{\Lambda} = 0.7$, with all uncertainties quoted at the 68.3% level, unless otherwise stated.

2. DATA

2.1. X-ray: *Chandra*

SPT J0417 was initially observed with the Chandra ACIS-I detector for 18 ks (after cleaning) in 2013. A follow-up observation conducted in 2023 using the ACIS-S detector added 85 ks of exposure. A combined total of 103 ks of clean time was analyzed using CIAO v4.16 and CALDB v4.11.0. Within r_{500} (990 kpc), the combined dataset contains an estimated 10,228 net counts in the 0.6 to 7.0 keV band, corresponding to a count rate of 0.0993 count s⁻¹.

The procedures for reducing and cleaning the Chandra data follow the guidelines provided in the Chandra Analysis Guide¹, as described in Mantz et al. (2015). In addition, we applied a time-dependent correction to the ancillary response files used in spectral modeling, as motivated by long-term calibration analyses of Abell 1795 over the course of the mission (Mantz et al. 2025).

Figure 1 displays the 0.6–7.0 keV Chandra X-ray image of SPT J0417, smoothed with a Gaussian kernel of 2-pixel (0.984 arcsec) radius, to emphasize the cluster's central region. The green circles denote the characteristic radii r_{2500} and r_{500} derived from the best-fitting Navarro-Frenk-White (NFW) mass model (Navarro et al. 1997) (see Section 3.1). The central panel presents a zoomed-in view of the X-ray image, highlighting a core morphology that is moderately peaked and exhibits slight asymmetry on scales of a few arcseconds. The right panel shows the Euclid image of the cluster core in SPT J0417 (Euclid Collaboration et al. 2025), revealing a massive red elliptical galaxy identified as the BCG (marked by the red cross), surrounded by similarly red elliptical galaxies.

From the X-ray image, we characterized the X-ray morphology of the cluster using the symmetry–peakiness–alignment (SPA) metrics of Mantz et al. (2015), which quantify the sharpness of the surface brightness peak (p), as well as the symmetry and alignment of elliptical isophotes (s and a). The analysis yielded $p = -0.688^{+0.009}_{-0.007}$, $s = 1.17^{+0.12}_{-0.10}$, and $a = 1.16^{+0.17}_{-0.09}$, firmly classifying the cluster as dynamically relaxed based on the relaxation thresholds of $p > -0.82$,

¹ https://cxc.harvard.edu/ciao/guides/acis_data.html

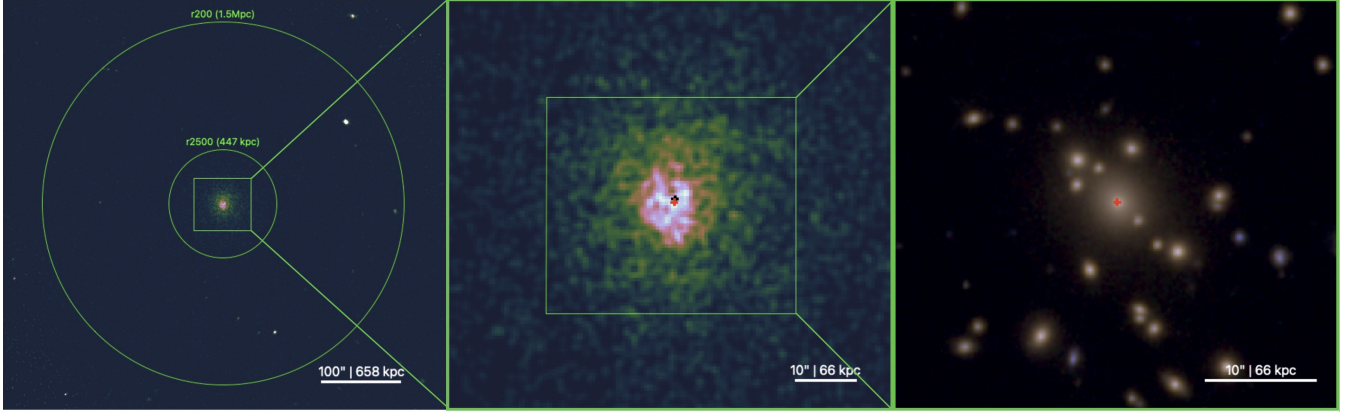


Figure 1. The left panel presents a 0.6–7.0 keV Chandra X-ray image of the cluster’s central region, constructed from raw pixels of $0.492 \times 0.492 \text{ arcsec}^2$ and smoothed with a Gaussian filter of 2-pixel (0.984 arcsec) radius. The red crosses indicate the location of the BCG. The SPA center from the morphological analysis is within $0.5''$ of the BCG center. The right panel displays the Euclid image (Euclid Collaboration et al. 2025), revealing a central red giant elliptical galaxy with other similarly red galaxies nearby.

$s > 0.87$, and $a > 1.00$. In Figure 2, this is illustrated by the red point (SPT J0417), which lies comfortably within the region of relaxed cluster (green points) in the SPA parameter space. We also find that the SPA center derived from the ICM morphology is offset by less than $0.5''$ from the BCG center, further supporting the classification of the system as dynamically relaxed.

2.2. Radio: ASKAP

For radio data, we used 1367 MHz observations from the Rapid ASKAP Continuum Survey (RACS) (Hale et al. 2021). RACS offers an angular resolution of $8''$ and provides uniform sensitivity ($\sim 0.3 \text{ mJy rms}$) across a large area of the sky (Duchesne et al. 2023). Three radio sources were detected by RACS at projected separations of approximately $13'', 28'', 44''$ from the BCG (Duchesne et al. 2024). The right panel of Figure 3 shows the 1.4 GHz ASKAP radio image, highlighting the three radio sources.

SPT J0417 is also included in the Dark Energy Survey (DES) Year 3 optically-selected “redMaPPer” cluster catalog (DES Collaboration et al. 2025). Each of the three ASKAP radio sources is associated with a confirmed cluster member galaxy, with positional offsets of less than $\sim 1.6''$, well below the RACS beam size. The assigned photometric redshifts of the matched member galaxies are 0.58 ± 0.02 (East object), 0.60 ± 0.02 (West object) and 0.59 ± 0.02 (North object) with cluster membership probabilities of 0.993, 0.995 and 0.995, respectively (DES Collaboration et al. 2025).

For the BCG, we report an upper limit on the radio luminosity of $\sim 1 \times 10^{40} \text{ erg s}^{-1}$, corresponding to three times the rms noise of the ASKAP map and following the approach of Calzadilla et al. (2024). This limit rules out the presence of particularly prominent relativistic

radio jets or a radio-luminous AGN in the central galaxy. However, radio emission below the current sensitivity cannot be excluded, as deeper observations have revealed BCGs hosting radio sources with luminosities below $10^{39} \text{ erg s}^{-1}$ (e.g., Veronica et al. 2025). More generally, AGN feedback in BCGs is expected to be episodic, with duty cycles shorter than 10^8 yr (Gaspari et al. 2017; Prasad et al. 2020), such that periods of low radio activity may fall below survey detection limits. Furthermore, while the highest mass BCGs are frequently radio-active, their luminosity can fluctuate by several orders of magnitudes over these timescales (Hogan et al. 2015; Main et al. 2017).

2.3. Infrared: Spitzer/WISE

SPT J0417 was observed using the *Spitzer Space Telescope* (PID 70053; PI Brodwin). Infrared photometry was obtained with IRAC (Fazio et al. 2004) in the $3.6 \mu\text{m}$ and $4.5 \mu\text{m}$ bands. Infrared-bright AGN in a cluster at $z \sim 0.58$ can be identified using a color criterion of $[3.6 \mu\text{m}] - [4.5 \mu\text{m}] \geq 0.61$ (Floyd et al., in prep.). Based on this criterion, neither the BCG nor the three ASKAP radio sources exhibit infrared colors consistent with an infrared-bright AGN. However, two additional galaxies in the vicinity exhibit IRAC colors consistent with infrared-bright AGN, located at RA = $04^{\text{h}}17^{\text{m}}22^{\text{s}}.74$, Dec = $-47^{\circ}50'43''$ and RA = $04^{\text{h}}17^{\text{m}}16^{\text{s}}.79$, Dec = $-47^{\circ}50'46''$, corresponding to projected cluster-centric distances of 0.743 Mpc and 0.863 Mpc, respectively. Both sources lie outside the field of view presented in the middle panel of Figure 3. An ongoing analysis is underway to assess whether these sources are cluster members or projected interlopers. The broader implications of AGN activity within the

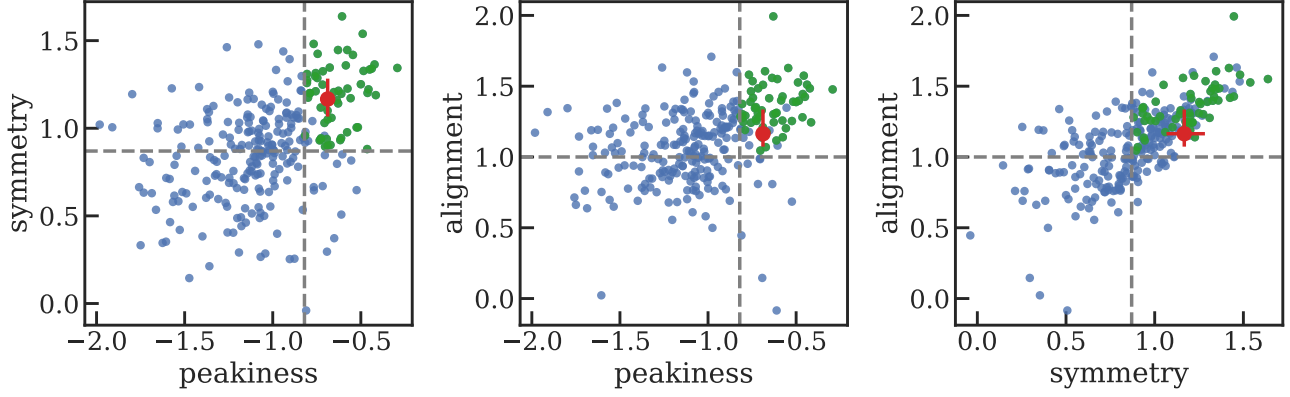


Figure 2. Distribution of X-ray peakiness (p), symmetry (s), and alignment (a) for clusters from Mantz et al. (2015). The dashed lines indicate the threshold used to define the relaxed sample. Clusters meeting all three criteria are shown in green, while non-relaxed clusters are plotted in blue. The red point marks SPT J0417, which lies well within the relaxed region.

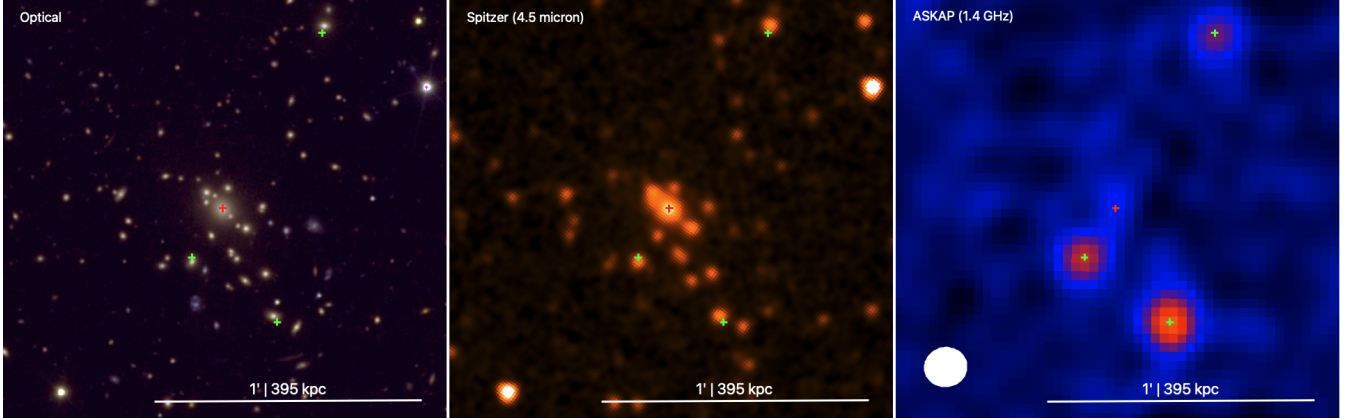


Figure 3. The left panel displays the optical image of the cluster from Euclid (Euclid Collaboration et al. 2025) for reference, with red crosses indicating the position of the BCG and green crosses marking the locations of detected radio sources. The middle panel shows the $4.5\ \mu\text{m}$ infrared image obtained with *Spitzer*, providing a view of the stellar and dust content. The right panel presents the $1.4\ \text{GHz}$ radio image from ASKAP with the beam size shown in the bottom left. Several radio sources are detected near the cluster center, but none is coincident with the BCG; instead, each is spatially associated with an optical counterpart confirmed to be a cluster member, making an association with the BCG unlikely. From these data, we derive a 3σ upper limit on the BCG radio luminosity of $\sim 1 \times 10^{40}\ \text{erg s}^{-1}$.

cluster environment will be discussed in Floyd et al. (in prep.).

The BCG was also observed with WISE, an all-sky infrared survey with imaging capabilities, at $3.4, 4.6, 12$, and $22\ \mu\text{m}$ (Wright et al. 2010). McDonald et al. (2016a) estimated the star formation rate (SFR) of the BCG by extrapolating a power-law fit from the observed $22\ \mu\text{m}$ data to the rest-frame $24\ \mu\text{m}$, following the method of Calzetti et al. (2007). The non-detection at $22\ \mu\text{m}$ sets an upper limit on the SFR of $28\ M_{\odot}\ \text{yr}^{-1}$.

2.4. Optical: Photometric Modeling

We investigated the star formation history of the BCG in SPT J0417 by fitting its spectral energy distribution (SED) using g, r, i, z, Y photometry from the Dark

Energy Survey DR2 (Abbott et al. 2021). The magnitude was first corrected for Galactic extinction in the direction of the BCG with $A_V = 0.0446$ (Schlafly & Finkbeiner 2011), applying the Cardelli et al. (1989) extinction curve and $R_V = 3.1$. The modeling was carried out with PROSPECTOR code (Johnson et al. 2021), adopting a Simple Stellar Population (SSP) template (Conroy et al. 2009; Conroy & Gunn 2010). In the fits, we assumed a Kroupa (2001) initial mass function (IMF) and parameterized internal dust attenuation using Kriek & Conroy (2013) model. Posterior distributions of total formed stellar mass, metallicity, and stellar population age were sampled with the EMCEE MCMC package (Foreman-Mackey et al. 2013). The resulting best-fit SSP spectrum and photometry are shown in Fig-

ure 4. The BCG is found to have a stellar metallicity of $\log_{10}(Z/Z_{\odot}) = -0.10^{+0.26}_{-0.23}$, a total formed stellar mass of $M_* = 9.5^{+1.2}_{-0.8} \times 10^{11} M_{\odot}$, and a stellar population age of $t_{\text{age}} = 3.0^{+0.8}_{-0.5}$ Gyr, with a reduced chi-squared value of $\chi^2_{\nu} = 0.69$. These results suggest that the bulk of the stellar mass in the BCG was assembled around $z = 1.25^{+0.33}_{-0.15}$, with little to no subsequent star formation over the past ~ 3 Gyr.

Additionally, McDonald et al. (2016a) obtained an optical spectrum of the BCG in SPT J0417 with the Inamori-Magellan Areal Camera and Spectrograph (IMACS) on the 6.5m Magellan Telescopes, targeting the redshifted [O II] emission line as a tracer of star formation in the central galaxy. No [O II] emission was detected, placing an upper limit on the star formation rate of $< 3.8 M_{\odot} \text{ yr}^{-1}$, consistent with negligible ongoing activity in the BCG. Taken together, these optical results indicate that the BCG in SPT J0417 has experienced no significant star formation during the past ~ 3 Gyr.

3. X-RAY ANALYSIS AND RESULTS

The results of our Chandra X-ray analysis are divided into four sections. Section 3.1 describes the spectral modeling framework adopted in the subsequent analysis. Section 3.2 details the thermodynamic structure of SPT J0417 through radial profiles of electron density, temperature, and metallicity. Section 3.3 explores the cooling properties of the intracluster medium, focusing on the pseudo-entropy, cooling time, and free-fall time. These results are based on an analysis that does not assume hydrostatic equilibrium, thereby minimizing potential biases in the temperature profile owing to the surface brightness morphology. Section 3.4 presents the results derived under the assumption of hydrostatic equilibrium and an NFW mass profile, providing measurements of the total mass, gas mass fraction, and concentration parameter. The characteristic radii r_{2500} and r_{500} , within which the overdensity is 2500 and 500 times the critical density of the universe, respectively, were adopted from the best-fitting NFW mass model and used consistently throughout the analysis. We further compare the properties of SPT J0417, measured within r_{500} , with a sample of 40 dynamically relaxed cool-core clusters from Mantz et al. (2016) (hereafter M16) via scaling relations.

3.1. Spectral Analysis and Modeling

For the spectral analysis, we used XSPEC to model the thermal emission from the hot ICM and the local Galactic halo using the APEC plasma model. Photoelectric absorption by Galactic gas was accounted for using the XSPEC PHABS model, with the hydrogen column

density fixed to $N_H = 1.28 \times 10^{20} \text{ cm}^{-2}$ (HI4PI Collaboration et al. 2016). We forward-modeled the three main components of foreground and background emission, namely diffuse Galactic emission, unresolved extragalactic sources and particle-induced backgrounds from cosmic-ray particles, following the methods described by Mantz et al. (2025). We adopt the BCG center, located at RA = $04^{\text{h}}17^{\text{m}}23^{\text{s}}.09$, Dec = $-47^{\circ}48'47''$, as the cluster center for our analysis.

Following the methodology of Mantz et al. (2014, 2016), we defined a set of annuli, spaced approximately logarithmically, extending from the cluster center to the radius where the cluster emission represents a 2σ excess over the background. The cluster is modeled as a series of concentric, isothermal, spherical shells with inner and outer radii corresponding to those of the annuli. The expected signal in each annulus was obtained by projecting the 3D model onto the plane of the sky. The density of each shell is constrained individually, whereas the temperature and metallicity are linked between groups of adjacent shells to improve the constraints on these parameters. Beyond $75''$, the cluster signal is no longer significantly detected over the background at most energies; therefore, spectral fitting is not performed, though we do use the integrated 1–2 keV surface brightness to constrain the gas density out to $150''$. This region is excluded from the visualization of the temperature and metallicity profiles (and related quantities) because the soft-band surface brightness alone does not provide useful constraints on these parameters in the relevant temperature and redshift regime.

We conducted two spectral analyses of the cluster: one using the non-parametric `projct` model in XSPEC, in which the ICM density and temperature profiles are a priori independent, and another in which these profiles are constrained under the assumption of hydrostatic equilibrium with an NFW mass profile, implemented using a modified version of the XSPEC `nfwmass` model (Mantz et al. 2014). Following Mantz et al. (2014), we exclude the central $14''$ or ~ 92 kpc region from the NFW-based analysis to mitigate the effects of potential deviations from the hydrostatic equilibrium, spherical symmetry, or the NFW mass model in this high signal-to-noise region. This exclusion radius is determined iteratively by increasing its size until the best-fitting NFW model parameters are stabilized.

3.2. Thermodynamical Profiles, Metallicity

As shown in the left panel of Figure 5, the electron density profile of the cluster features a core in the innermost bin, corresponding to the central $2''$ with a peak density of $0.08 \pm 0.01 \text{ cm}^{-3}$. This value is typical

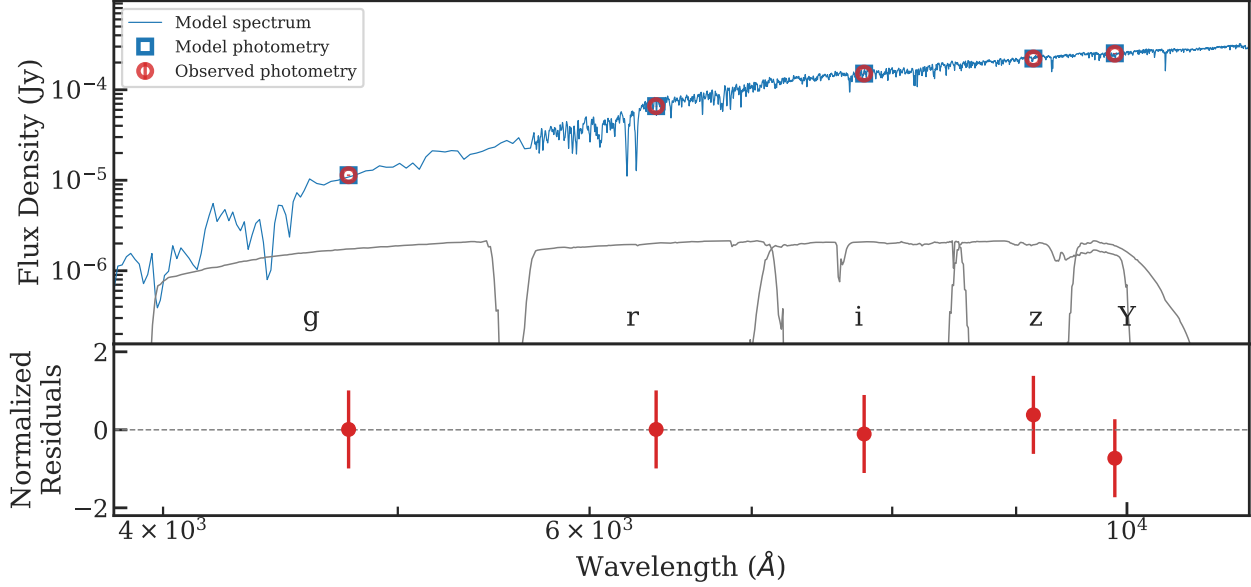


Figure 4. Top: Observed-frame optical photometry of the BCG in SPT J0417 (DECam g, r, i, z, Y ; red points with error bars) compared with the best-fit simple stellar population (SSP) model derived using PROSPECTOR. The model spectrum is shown in blue, with the corresponding synthetic photometry indicated by blue squares. The relative transmission curves of each filter are shown in gray for reference. Bottom: Residuals normalized to the photometric uncertainties. The fit is consistent with an old stellar population in the BCG, with little or no evidence of star formation within the last ~ 3 Gyr.

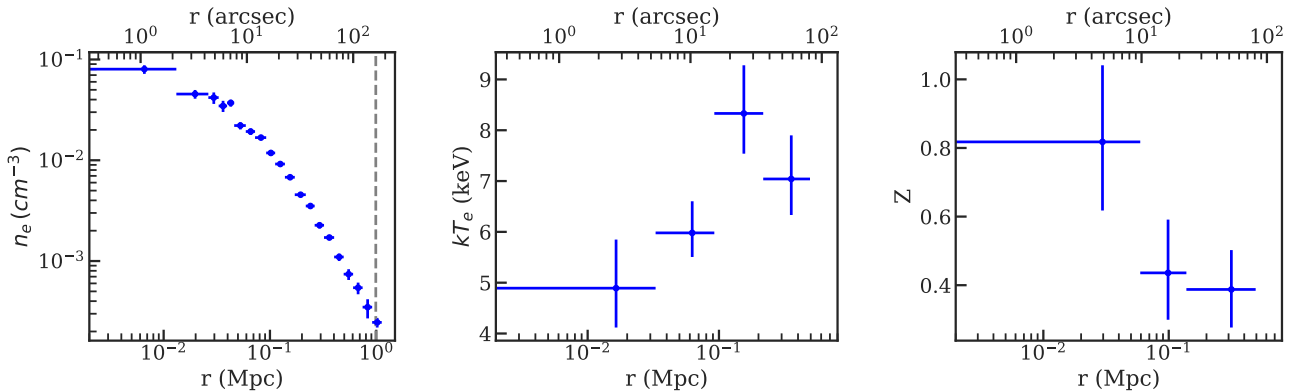


Figure 5. Deprojected ICM thermodynamic profiles of SPT J0417. Left: Electron density profile, with the gray dashed line marking R_{500} . Middle: Temperature profile showing a clear increase in temperature from the core to the outskirts. Right: Metallicity profile, displaying an enhancement near the cluster core, while the outer regions are consistent with an average metallicity of ~ 0.3 solar (Mernier et al. 2017).

when compared to the 40 dynamically relaxed cool-core clusters from M16 (see Fig. 6). Owing to the limited number of photons in this region, we combined the first two bins to obtain a single central $2''$ bin with sufficient signal-to-noise. Deeper observations will be necessary to achieve higher spatial resolution and to resolve the structure within the central few arcseconds.

In addition, the middle panel of Figure 5 presents the temperature profile, which indicates the presence of a

strong cool core. The temperature rises steeply from a minimum of $4.8_{-0.8}^{+1.0}$ keV at ~ 20 kpc to a maximum of $8.3_{-0.8}^{+0.9}$ keV at ~ 200 kpc. The temperature profile remains well-constrained out to $0.5r_{500}$, where r_{500} is located at ~ 0.99 Mpc.

Finally, the right panel of Figure 5 presents the deprojected radial profile of the ICM iron abundance, in solar units (Asplund et al. 2009). The metallicity profile exhibits a clear radial gradient, decreasing from 0.8 ± 0.2

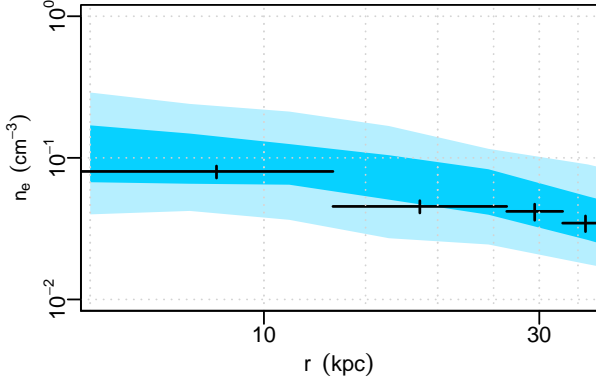


Figure 6. Zoom-in view of the central electron density profile of SPT J0417 (black), shown as a function of radius, compared with the 68.3% and 95.4% confidence ranges of the physical density profiles from the M16 sample.

solar in the central $r < 60$ kpc to 0.39 ± 0.11 solar in the outer regions. This outer value is consistent with the average core-excised metallicity observed in lower redshift galaxy clusters (~ 0.3 solar) and is consistent with the picture in which the accreting gas at large radii is pre-enriched to 0.3 solar, likely through early feedback processes or galactic winds (Werner et al. 2013; Urban et al. 2017). The elevated central abundance, on the other hand, is likely to reflect additional enrichment from star formation within the central cluster galaxies, as well as from the infalling cores of subhalos that deposit metal-rich gas into the cluster center during merger events. (Leccardi & Molendi 2008; Ettori et al. 2015; McDonald et al. 2016b; Mernier et al. 2017; Mantz et al. 2017).

3.3. Pseudo-Entropy, Cooling Time, Free-fall Time

Several key properties were calculated to investigate the heating and cooling mechanisms within the ICM, including pseudo-entropy, cooling time, and free-fall time. These quantities provide insights into the thermal history and stability of the cluster core.

After obtaining the electron density and temperature profiles, the pseudo-entropy of the ICM is derived using

$$K(r) = kT(r) \times n_e(r)^{-2/3}, \quad (1)$$

(Balogh et al. 1999; Ponman et al. 1999) where $kT(r)$ is the temperature profile, and $n_e(r)$ is the electron density profile. Pseudo-entropy serves as a key observable for studying the effects of feedback in clusters, as the thermal history of a cluster is governed solely by heat gains and losses (Cavagnolo et al. 2009; Panagoulia et al. 2014). In the absence of feedback mechanisms, the pseudo-entropy profile is expected to increase monotonically with radius (Voit 2005; Cavagnolo et al. 2009).

The left panel of Figure 7 shows the radial pseudo-entropy profile derived from the deprojection analysis. Within the central $r < 13$ kpc, the pseudo-entropy in the innermost bins is measured to be 26_{-5}^{+6} keV cm 2 . At large radii, the pseudo-entropy profile exhibits the expected power-law increase, consistent with predictions from numerical simulations (Voit et al. 2002, 2005) and observations of other clusters (e.g., Su et al. 2015; Tchernin et al. 2016), for which the ICM entropy profile typically scales as $\propto r^{1.1}$.

The cooling time is typically defined in terms of the specific heat in constant volume as

$$t_{\text{cool}} = \frac{3}{2} \frac{(n_e + n_p) k T(r)}{n_e n_p \Lambda(T)}, \quad (2)$$

where $\Lambda(T)$ is the cooling function at temperature T , calculated using the metallicity derived from our spectral analysis (Sutherland & Dopita 1993), and n_e and n_p are the electron and proton number densities, respectively. The central cooling time, often defined as the cooling time within the innermost ~ 10 kpc, serves as a key diagnostic tool for distinguishing between cool-core and non-cool-core clusters. As shown in the right panel of Figure 7, the central cooling time measured within the innermost annulus ($r < 13$ kpc) is 515_{-75}^{+96} Myr, falling below the 1 Gyr threshold commonly used to classify a system as a cool-core cluster (Hudson et al. 2010).

An additional quantity of interest is the free-fall time, t_{ff} , which characterizes the timescale for gas to collapse under gravity and is defined as $t_{\text{ff}} = (2r/g)^{1/2}$, where g is the local gravitational acceleration at radius r . Thermal instability and subsequent cooling of the ICM, leading to the formation of molecular gas and new stars, are observed to occur when the ratio $t_{\text{cool}}/t_{\text{ff}}$ drops below a critical value of approximately 10 (Gaspari et al. 2012; Sharma et al. 2012). This cooling process can, in turn, fuel feedback from AGN, which reheats the core, suppresses further cooling, and thereby initiates a self-regulating feedback cycle (Voit et al. 2015; Li et al. 2015). This behavior has been reproduced in simulations, which typically yield a minimum $t_{\text{cool}}/t_{\text{ff}} > 10$ (Gaspari et al. 2012, 2013; Li et al. 2015), and is also supported by observations of cool-core clusters exhibiting nebular emission, where the inner $t_{\text{cool}}/t_{\text{ff}}$ approaches, but does not fall below, this threshold (Voit et al. 2015; Hogan et al. 2017; Pulido et al. 2018). Notably, the Phoenix cluster is the only known exception to this trend, exhibiting $t_{\text{cool}}/t_{\text{ff}}$ values approaching unity on kpc scales, while simultaneously hosting substantial star formation in its central galaxy (McDonald et al. 2019). In the case of SPT J0417, we find that $t_{\text{cool}}/t_{\text{ff}}$ profile does not fall below the critical threshold of ~ 10

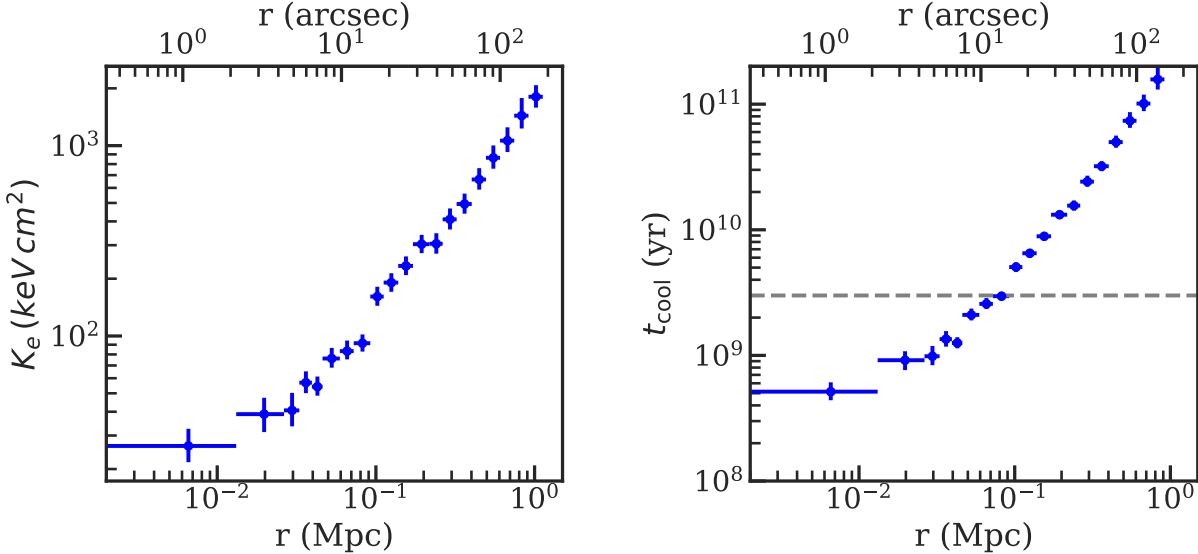


Figure 7. Left: Deprojected pseudo-entropy profile of SPT J0417. Right: Radial profile of the ICM cooling time. The grey dashed line marks 3 Gyr, which we use to define the cooling radius r_{cool} , as the radius where the cooling time drops below this threshold, for comparison with literature values. The entropy decline to below ~ 30 keV cm 2 in the core, together with a central cooling time shorter than 1 Gyr, classifies this system as a cool-core cluster (Hudson et al. 2010). We note that, owing to the limited data, the innermost temperature bin corresponds to ~ 30 kpc. This results in an artificially flat temperature profile in the core, leading to an overestimate of the central pseudo-entropy and cooling time, as the true temperature is expected to decline further toward the cluster center.

at any radius, which is consistent with the presence of a self-regulated AGN feedback mechanism.

To further quantify the cooling properties, we estimated the classically inferred ICM cooling rate using $\dot{M}_{\text{cool}} = M_{\text{gas}}(r < r_{\text{cool}})/t_{\text{cool}}$, where r_{cool} is the radius at which the cooling time falls below 3 Gyr, corresponding to 85 ± 4 kpc. Following the convention of McDonald et al. (2018), we adopt a cooling time threshold of 3 Gyr to describe the region of the cluster core where cooling is most relevant. Under this definition, we derive a cooling rate of $560 \pm 70 M_{\odot} \text{ yr}^{-1}$. When compared to the upper limit on the star formation rate of $3.8 M_{\odot} \text{ yr}^{-1}$, this implies a cooling efficiency, defined as $\epsilon_{\text{cool}} = \text{SFR}/\dot{M}_{\text{cool}}$, of less than 0.7%. This value falls within the typical range observed for galaxy clusters (0.3%–5.8%; Calzadilla et al. 2022), indicating that SPT J0417 is consistent with a quenched system, similar to the majority of the cluster population.

Figure 8 compares the scaled thermodynamic profiles of SPT J0417 (electron density, temperature, pseudo-entropy and cooling time) with those of 40 other dynamically relaxed, cool-core clusters from M16 (cyan band), spanning a redshift range of 0.078–1.063. Radii are scaled by r_{2500} , and the profiles are scaled for the redshift and mass dependence predicted by self similarity. In comparison to this sample, SPT J0417 appears

broadly consistent, exhibiting the characteristics of a typical dynamically relaxed, cool-core cluster from its inner core out to the outskirts, with central values in good agreement with the comparison set. Note that the innermost temperature bin extends to ~ 30 kpc, which may slightly overestimate the central pseudo-entropy and cooling time (see Figure 7).

Several diagnostic criteria predict the conditions under which multiphase cooling occurs in ICM. For instance, Cavagnolo et al. (2008) identified either a central pseudo-entropy threshold of 30 keV cm 2 , or $t_{\text{cool}} \approx 1$ Gyr, below which strong cooling and significant star formation rates are typically observed. In the case of SPT J0417, the core pseudo-entropy and central cooling time approach these thresholds, suggesting the potential for cooling or star formation near the central galaxy of the cluster to occur. However, no evidence for any star formation is detected in the optical spectrum of the central galaxy.

3.4. Results from Mass Modeling and Scaling Relations

In this section, we utilize the `nfwmass` model within XSPEC, assuming an NFW mass profile and hydrostatic equilibrium, to constrain the characteristic radius, total mass, gas mass fraction, and NFW concentration parameter, defined as $c = r_{200}/r_s$.

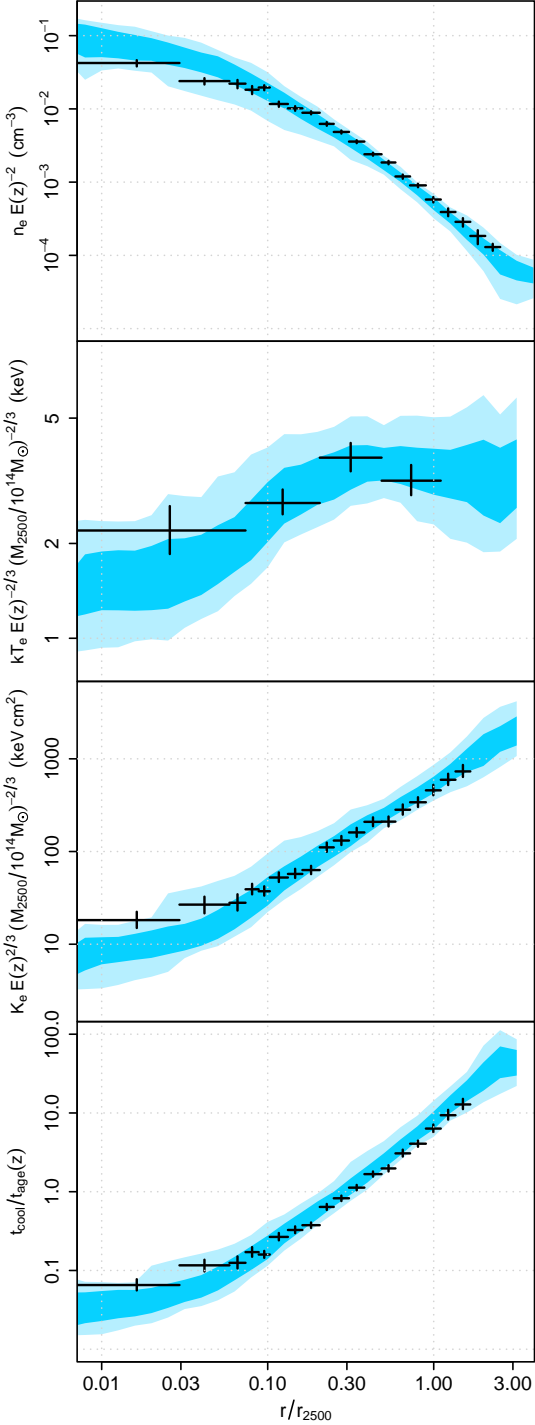


Figure 8. Scaled electron density, temperature, pseudo-entropy, and cooling time profiles as a function of scaled radius for SPT J0417 (cyan) compared to the 68.3% and 95.4% confidence regions of a larger sample of relaxed, cool-core clusters spanning a redshift range of 0.078–1.063 of the M16 sample. Relative to this sample, the overall profile shapes of SPT J0417 remain consistent with the general trends observed across the larger sample at various redshifts.

We measure the gas mass fraction, $f_{\text{gas}} = M_{\text{gas}}/M_{\text{tot}}$, within a spherical shell spanning 0.8 – $1.2 r_{2500}$ to be $0.13^{+0.01}_{-0.02}$, consistent with the measurements of other clusters at similar redshifts (Mantz et al. 2022). The NFW concentration parameter for SPT J0417 was determined to be $4.9^{+0.8}_{-0.5}$, in agreement with the typical values observed for massive clusters at comparable redshifts (Darragh-Ford et al. 2023). Together, these results suggest that, on large scales, SPT J0417 exhibits properties characteristic of a typical strong cool-core dynamically relaxed cluster, standard gas mass fraction, and concentration consistent with the massive relaxed cluster population.

Table 1 summarizes our measurements of the global properties of SPT J0417 derived from the X-ray analysis employing the NFWMASS and PROJCT models, as described. Reported quantities include characteristic masses (M_{500} , M_{200}), and characteristic radius (r_{500}), the core-excised X-ray temperature measured within 0.15 – $1.0 r_{500}$, and the total X-ray luminosity (L_X) converted to the 0.1 – 2.4 keV rest-frame band. To place these measurements in a broader context, we compare them with the relaxed cluster sample of M16, and recent results for SPT-CL J2215-3537 (in red; Stueber et al. 2026), in Figure 9. This figure presents scaling relations between the characteristic mass, gas mass, average temperature, total luminosity, and core-excised luminosity within r_{500} , with temperatures and core-excised luminosities excluding the central $< 0.15 r_{500}$. Clusters from the M16 sample are color-coded by redshift, whereas SPT J0417 is marked in black. The gray shaded regions indicate the 1σ predictive intervals from a power-law fit to the M16 sample, incorporating intrinsic log-normal scatter. Across all properties, SPT J0417 lies within the expected range for massive, relaxed, cool-core clusters over a redshift span of 0.078 – 1.063 (Mantz et al. 2016).

4. CONCLUSION

In this study, we present new deep ~ 100 ks observations of SPT J0417 using the Chandra X-ray Observatory. Our key findings are as follows:

1. The large-scale X-ray morphology of SPT J0417 is consistent with a dynamically relaxed system, as indicated by the SPA criteria (Mantz et al. 2015). Its global properties, including the total X-ray luminosity (L_X), total mass (M_{500}), gas mass fraction, and concentration parameter, are broadly consistent with those of typical massive, relaxed, cool-core clusters.

Table 1. Global properties of SPT J0417

z	r_{500} (Mpc)	M_{500} ($10^{14} M_{\odot}$)	M_{200} ($10^{14} M_{\odot}$)	M_{gas} ($10^{13} M_{\odot}$)	kT (keV)	L_X (0.1-2.4 keV) ($10^{44} \text{ erg s}^{-1}$)
0.581	$0.99^{+0.05}_{-0.06}$	$5.0^{+1.1}_{-0.7}$	$6.9^{+1.6}_{-1.1}$	$7.4^{+0.5}_{-0.5}$	$7.4^{+0.6}_{-0.5}$	10.8 ± 0.3

NOTE—Where applicable, measurements are referenced to the characteristic radius r_{500} . The X-ray temperature (kT) is extracted from the region excluding the cluster core, specifically from $0.15-1 r_{500}$.

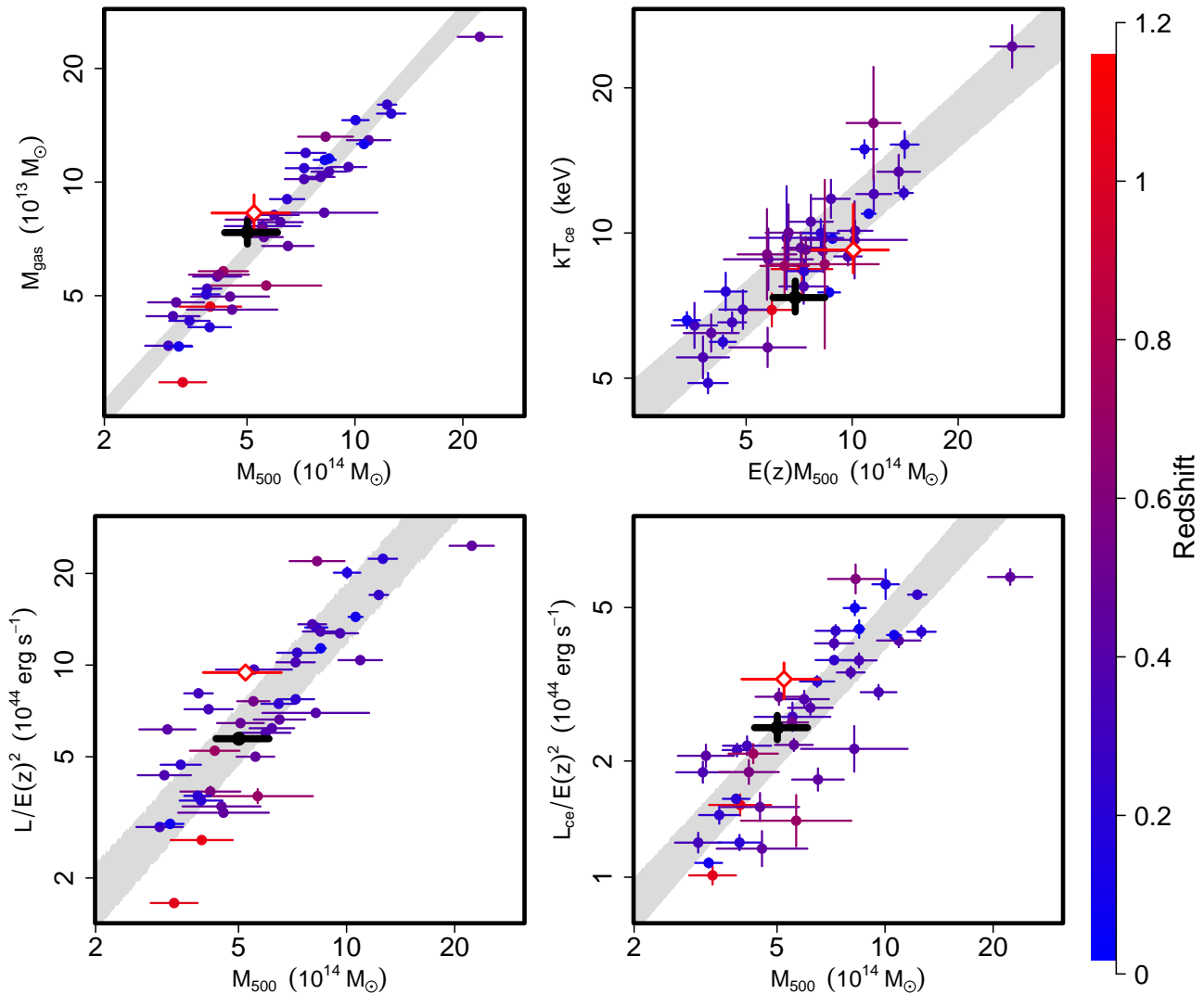


Figure 9. Scatter plots of the integrated thermodynamic quantities for SPT J0417 (black points) are shown in comparison with the relaxed cluster sample from M16, along with SPT-CL J2215-3537 (white-centered red diamond; Stueber et al. 2026). The M16 clusters are color-coded by redshift, as indicated by the color bar. The shaded regions represent the 1σ predictive intervals derived from a power-law fit to the M16 data, accounting for intrinsic log-normal scatter.

2. The peak ICM density in the core is measured to be $0.08 \pm 0.01 \text{ cm}^{-3}$, also typical of cool-core clusters.

ters. The central pseudo-entropy ($26^{+6}_{-5} \text{ keV cm}^2$) and central cooling time ($515^{+96}_{-75} \text{ Myr}$) fall below

the thresholds of ~ 30 keV cm 2 and ~ 1 Gyr, respectively, suggesting strong cooling in the core and conditions that could support significant star formation.

3. Both SED fitting of the BCG photometry and the non-detection of [O II] emission in its optical spectrum indicate an absence of recent or ongoing star formation, with the majority of the stellar population formed at $z \sim 1.25$ and no significant activity over the past ~ 3 Gyr. These results suggest that cooling in the cluster core has been suppressed to levels insufficient to sustain detectable star formation. In addition, ASKAP radio and Spitzer infrared data show no evidence for strong ongoing AGN activity in the BCG.

SPT J0417 represents another example of a massive dynamically relaxed, cool-core cluster with a tight upper limit on ongoing or recent star formation in its central galaxy. Comparable systems include Abell 2029, a massive relaxed galaxy cluster at $z = 0.07795$ with only minimal star formation ($0.03\text{--}0.06 M_{\odot} \text{ yr}^{-1}$), as measured with GALEX (Hicks et al. 2010), and MS2137-2353 at $z = 0.313$, which hosts a BCG with a star formation rate of $\sim 2 M_{\odot} \text{ yr}^{-1}$ (Cooke et al. 2016). SPT J0417 extends this population to higher redshift, while maintaining a comparable mass and similar central thermodynamic properties. Such systems stand in contrast to scenarios predicting that the most massive cool-core clusters should exhibit high star formation rates ($>100 M_{\odot} \text{ yr}^{-1}$) due to saturation of AGN feedback heating.

One possible explanation for the lack of star formation in SPT J0417 is hot-mode accretion. In this scenario, the AGN is fueled not by cool gas but by the surrounding hot ICM. While accretion from hot gas alone is generally insufficient to balance ICM cooling, a sufficiently massive central supermassive black hole, with a mass $\sim 10^{10} M_{\odot}$, could produce feedback powerful enough to suppress cooling and prevent cold gas formation. Further studies of BCG properties, particularly SMBH masses in relaxed clusters with and without ongoing star formation, will be critical to test this scenario, with SPT J0417 providing an important intermediate-redshift case study of this class of systems.

Finally, deeper and higher spatial resolution radio and deeper X-ray observations of the inner few arcseconds of the cluster are needed to probe AGN activity in the BCG and to search for subtle ICM features such as sloshing or cold fronts in the core. In addition, complementary

rest-frame optical and near-infrared spectroscopy with facilities such as the Hubble Space Telescope and the James Webb Space Telescope will also be essential for constraining any residual star formation in the BCG, offering new insight into the processes that regulate cooling and feedback in massive clusters.

5. ACKNOWLEDGMENTS

TS acknowledges support from the Kavli Postdoctoral Fellowship at Stanford University and from the grants for the development of new faculty staff, Ratchadapiseksomphot Fund, Chulalongkorn University.

This research has made use of data obtained from the Chandra Data Archive provided by the Chandra X-ray Center (CXC). Support for this work was provided by the National Aeronautics and Space Administration through Chandra Award Number GO3-24113X issued by the Chandra X-ray Center, which is operated by the Smithsonian Astrophysical Observatory on behalf of the National Aeronautics Space Administration under contract NAS8-03060. This paper employs a list of Chandra datasets, obtained by the Chandra X-ray Observatory, contained in the Chandra Data Collection (CDC) ‘378’ doi:10.25574/cdc.378. We acknowledge support from the U.S. Department of Energy under contract number DE-AC02-76SF00515.

This work was performed in the context of the South Pole Telescope scientific program. The South Pole Telescope program is supported by the National Science Foundation (NSF) through awards OPP-1852617 and OPP-2332483. Partial support is also provided by the NSF Physics Frontier Center grant PHY-0114422 to the Kavli Institute of Cosmological Physics at the University of Chicago, the Kavli Foundation and the Gordon and Betty Moore Foundation grant GBMF 947 to the University of Chicago. The SPT is also supported by the U.S. Department of Energy. Argonne National Laboratory’s work was supported by the U.S. Department of Energy, Office of High Energy Physics, under contract DE-AC02-06CH11357.

Facilities: CXO, Spitzer, WISE, ASKAP, Magellan 6.5m telescopes (Baade/IMACS)

Software: astropy (Astropy Collaboration et al. 2013, 2018, 2022), CIAO (CIAO Development Team 2013; Fruscione et al. 2006), MARX (Wise et al. 2013; Davis et al. 2012), LMC (Mantz 2017), HEASOFT (NASA High Energy Astrophysics Science Archive Research Center (Heasarc) 2014), SXRBG (Sabol & Snowden 2019), XSPEC (Arnaud et al. 1999; Arnaud 1996)

REFERENCES

Abbott, T. M. C., Adamów, M., Aguena, M., et al. 2021, *ApJS*, 255, 20, doi: [10.3847/1538-4365/ac00b3](https://doi.org/10.3847/1538-4365/ac00b3)

Allen, S. W., Schmidt, R. W., & Fabian, A. C. 2001, *MNRAS*, 328, L37, doi: [10.1046/j.1365-8711.2001.05079.x](https://doi.org/10.1046/j.1365-8711.2001.05079.x)

Arnaud, K., Dorman, B., & Gordon, C. 1999, XSPEC: An X-ray spectral fitting package, *Astrophysics Source Code Library*, record ascl:9910.005

Arnaud, K. A. 1996, in *Astronomical Society of the Pacific Conference Series*, Vol. 101, *Astronomical Data Analysis Software and Systems V*, ed. G. H. Jacoby & J. Barnes, 17

Asplund, M., Grevesse, N., Sauval, A. J., & Scott, P. 2009, *ARA&A*, 47, 481, doi: [10.1146/annurev.astro.46.060407.145222](https://doi.org/10.1146/annurev.astro.46.060407.145222)

Astropy Collaboration, Robitaille, T. P., Tollerud, E. J., et al. 2013, *A&A*, 558, A33, doi: [10.1051/0004-6361/201322068](https://doi.org/10.1051/0004-6361/201322068)

Astropy Collaboration, Price-Whelan, A. M., Sipócz, B. M., et al. 2018, *AJ*, 156, 123, doi: [10.3847/1538-3881/aabc4f](https://doi.org/10.3847/1538-3881/aabc4f)

Astropy Collaboration, Price-Whelan, A. M., Lim, P. L., et al. 2022, *ApJ*, 935, 167, doi: [10.3847/1538-4357/ac7c74](https://doi.org/10.3847/1538-4357/ac7c74)

Balogh, M. L., Babul, A., & Patton, D. R. 1999, *Monthly Notices of the Royal Astronomical Society*, 307, 463, doi: [10.1046/j.1365-8711.1999.02608.x](https://doi.org/10.1046/j.1365-8711.1999.02608.x)

Bleem, L. E., Stalder, B., de Haan, T., et al. 2015, *ApJS*, 216, 27, doi: [10.1088/0067-0049/216/2/27](https://doi.org/10.1088/0067-0049/216/2/27)

Calzadilla, M. S., McDonald, M., Donahue, M., et al. 2022, *ApJ*, 940, 140, doi: [10.3847/1538-4357/ac9790](https://doi.org/10.3847/1538-4357/ac9790)

Calzadilla, M. S., McDonald, M., Benson, B. A., et al. 2024, *ApJ*, 976, 169, doi: [10.3847/1538-4357/ad8916](https://doi.org/10.3847/1538-4357/ad8916)

Calzetti, D., Kennicutt, R. C., Engelbracht, C. W., et al. 2007, *ApJ*, 666, 870, doi: [10.1086/520082](https://doi.org/10.1086/520082)

Cardelli, J. A., Clayton, G. C., & Mathis, J. S. 1989, *ApJ*, 345, 245, doi: [10.1086/167900](https://doi.org/10.1086/167900)

Cavagnolo, K. W., Donahue, M., Voit, G. M., & Sun, M. 2008, *ApJL*, 683, L107, doi: [10.1086/591665](https://doi.org/10.1086/591665)

—. 2009, *ApJS*, 182, 12, doi: [10.1088/0067-0049/182/1/12](https://doi.org/10.1088/0067-0049/182/1/12)

CIAO Development Team. 2013, CIAO: Chandra Interactive Analysis of Observations, *Astrophysics Source Code Library*, record ascl:1311.006

Conroy, C., & Gunn, J. E. 2010, *ApJ*, 712, 833, doi: [10.1088/0004-637X/712/2/833](https://doi.org/10.1088/0004-637X/712/2/833)

Conroy, C., Gunn, J. E., & White, M. 2009, *ApJ*, 699, 486, doi: [10.1088/0004-637X/699/1/486](https://doi.org/10.1088/0004-637X/699/1/486)

Cooke, K. C., O'Dea, C. P., Baum, S. A., et al. 2016, *ApJ*, 833, 224, doi: [10.3847/1538-4357/833/2/224](https://doi.org/10.3847/1538-4357/833/2/224)

Darragh-Ford, E., Mantz, A. B., Rasia, E., et al. 2023, *MNRAS*, 521, 790, doi: [10.1093/mnras/stad585](https://doi.org/10.1093/mnras/stad585)

Davis, J. E., Bautz, M. W., Dewey, D., et al. 2012, in *Society of Photo-Optical Instrumentation Engineers (SPIE) Conference Series*, Vol. 8443, *Space Telescopes and Instrumentation 2012: Ultraviolet to Gamma Ray*, ed. T. Takahashi, S. S. Murray, & J.-W. A. den Herder, 84431A, doi: [10.1117/12.926937](https://doi.org/10.1117/12.926937)

DES Collaboration, Abbott, T. M. C., Aguena, M., et al. 2025, arXiv e-prints, arXiv:2503.13632, doi: [10.48550/arXiv.2503.13632](https://doi.org/10.48550/arXiv.2503.13632)

Donahue, M., Connor, T., Fogarty, K., et al. 2015, *ApJ*, 805, 177, doi: [10.1088/0004-637X/805/2/177](https://doi.org/10.1088/0004-637X/805/2/177)

Duchesne, S. W., Thomson, A. J. M., Pritchard, J., et al. 2023, *PASA*, 40, e034, doi: [10.1017/pasa.2023.31](https://doi.org/10.1017/pasa.2023.31)

Duchesne, S. W., Grundy, J. A., Heald, G. H., et al. 2024, *PASA*, 41, e003, doi: [10.1017/pasa.2023.60](https://doi.org/10.1017/pasa.2023.60)

Edge, A. C., Stewart, G. C., & Fabian, A. C. 1992, *MNRAS*, 258, 177, doi: [10.1093/mnras/258.1.177](https://doi.org/10.1093/mnras/258.1.177)

Ettori, S., Baldi, A., Balestra, I., et al. 2015, *A&A*, 578, A46, doi: [10.1051/0004-6361/201425470](https://doi.org/10.1051/0004-6361/201425470)

Euclid Collaboration, Mellier, Y., Abdurro'uf, et al. 2025, *A&A*, 697, A1, doi: [10.1051/0004-6361/202450810](https://doi.org/10.1051/0004-6361/202450810)

Fabian, A. C. 1994, *ARA&A*, 32, 277, doi: [10.1146/annurev.aa.32.090194.001425](https://doi.org/10.1146/annurev.aa.32.090194.001425)

—. 2012, *ARA&A*, 50, 455, doi: [10.1146/annurev-astro-081811-125521](https://doi.org/10.1146/annurev-astro-081811-125521)

Fabian, A. C., & Nulsen, P. E. J. 1977, *MNRAS*, 180, 479, doi: [10.1093/mnras/180.3.479](https://doi.org/10.1093/mnras/180.3.479)

Fazio, G. G., Hora, J. L., Allen, L. E., et al. 2004, *ApJS*, 154, 10, doi: [10.1086/422843](https://doi.org/10.1086/422843)

Foreman-Mackey, D., Hogg, D. W., Lang, D., & Goodman, J. 2013, *PASP*, 125, 306, doi: [10.1086/670067](https://doi.org/10.1086/670067)

Fraser-McKelvie, A., Brown, M. J. I., & Pimbblet, K. A. 2014, *MNRAS*, 444, L63, doi: [10.1093/mnrasl/slu117](https://doi.org/10.1093/mnrasl/slu117)

Fruscione, A., McDowell, J. C., Allen, G. E., et al. 2006, in *Society of Photo-Optical Instrumentation Engineers (SPIE) Conference Series*, Vol. 6270, *Observatory Operations: Strategies, Processes, and Systems*, ed. D. R. Silva & R. E. Doxsey, 62701V, doi: [10.1117/12.671760](https://doi.org/10.1117/12.671760)

Gaspari, M., Brighenti, F., & Ruszkowski, M. 2013, *Astronomische Nachrichten*, 334, 394, doi: [10.1002/asna.201211865](https://doi.org/10.1002/asna.201211865)

Gaspari, M., Ruszkowski, M., & Sharma, P. 2012, *ApJ*, 746, 94, doi: [10.1088/0004-637X/746/1/94](https://doi.org/10.1088/0004-637X/746/1/94)

Gaspari, M., Temi, P., & Brighenti, F. 2017, *MNRAS*, 466, 677, doi: [10.1093/mnras/stw3108](https://doi.org/10.1093/mnras/stw3108)

Hale, C. L., McConnell, D., Thomson, A. J. M., et al. 2021, *PASA*, 38, e058, doi: [10.1017/pasa.2021.47](https://doi.org/10.1017/pasa.2021.47)

HI4PI Collaboration, Ben Bekhti, N., Flöer, L., et al. 2016, *A&A*, 594, A116, doi: [10.1051/0004-6361/201629178](https://doi.org/10.1051/0004-6361/201629178)

Hicks, A. K., Mushotzky, R., & Donahue, M. 2010, *ApJ*, 719, 1844, doi: [10.1088/0004-637X/719/2/1844](https://doi.org/10.1088/0004-637X/719/2/1844)

Hlavacek-Larrondo, J., Fabian, A. C., Edge, A. C., et al. 2013, *MNRAS*, 431, 1638, doi: [10.1093/mnras/stt283](https://doi.org/10.1093/mnras/stt283)

Hogan, M. T., Edge, A. C., Geach, J. E., et al. 2015, *MNRAS*, 453, 1223, doi: [10.1093/mnras/stv1518](https://doi.org/10.1093/mnras/stv1518)

Hogan, M. T., McNamara, B. R., Pulido, F. A., et al. 2017, *ApJ*, 851, 66, doi: [10.3847/1538-4357/aa9af3](https://doi.org/10.3847/1538-4357/aa9af3)

Hudson, D. S., Mittal, R., Reiprich, T. H., et al. 2010, *A&A*, 513, A37, doi: [10.1051/0004-6361/200912377](https://doi.org/10.1051/0004-6361/200912377)

Johnson, B. D., Leja, J., Conroy, C., & Speagle, J. S. 2021, *ApJS*, 254, 22, doi: [10.3847/1538-4365/abef67](https://doi.org/10.3847/1538-4365/abef67)

Kriek, M., & Conroy, C. 2013, *ApJL*, 775, L16, doi: [10.1088/2041-8205/775/1/L16](https://doi.org/10.1088/2041-8205/775/1/L16)

Kroupa, P. 2001, *MNRAS*, 322, 231, doi: [10.1046/j.1365-8711.2001.04022.x](https://doi.org/10.1046/j.1365-8711.2001.04022.x)

Leccardi, A., & Molendi, S. 2008, *A&A*, 487, 461, doi: [10.1051/0004-6361:200810113](https://doi.org/10.1051/0004-6361:200810113)

Li, Y., Bryan, G. L., Ruszkowski, M., et al. 2015, *ApJ*, 811, 73, doi: [10.1088/0004-637X/811/2/73](https://doi.org/10.1088/0004-637X/811/2/73)

Main, R. A., McNamara, B. R., Nulsen, P. E. J., Russell, H. R., & Vantyghem, A. N. 2017, *MNRAS*, 464, 4360, doi: [10.1093/mnras/stw2644](https://doi.org/10.1093/mnras/stw2644)

Mantz, A. B. 2017, LMC: Logarithmantic Monte Carlo, Astrophysics Source Code Library, record ascl:1706.005

Mantz, A. B., Allen, S. W., Morris, R. G., et al. 2014, *MNRAS*, 440, 2077, doi: [10.1093/mnras/stu368](https://doi.org/10.1093/mnras/stu368)

Mantz, A. B., Allen, S. W., Morris, R. G., & Schmidt, R. W. 2016, *MNRAS*, 456, 4020, doi: [10.1093/mnras/stv2899](https://doi.org/10.1093/mnras/stv2899)

Mantz, A. B., Allen, S. W., Morris, R. G., et al. 2015, *MNRAS*, 449, 199, doi: [10.1093/mnras/stv219](https://doi.org/10.1093/mnras/stv219)

—. 2017, *MNRAS*, 472, 2877, doi: [10.1093/mnras/stx2200](https://doi.org/10.1093/mnras/stx2200)

Mantz, A. B., Flores, A. M., Somboonpanyakul, T., et al. 2025, arXiv e-prints, arXiv:2512.05405, doi: [10.48550/arXiv.2512.05405](https://doi.org/10.48550/arXiv.2512.05405)

Mantz, A. B., Morris, R. G., Allen, S. W., et al. 2022, *MNRAS*, 510, 131, doi: [10.1093/mnras/stab3390](https://doi.org/10.1093/mnras/stab3390)

McDonald, M., Gaspari, M., McNamara, B. R., & Tremblay, G. R. 2018, *ApJ*, 858, 45, doi: [10.3847/1538-4357/aabace](https://doi.org/10.3847/1538-4357/aabace)

McDonald, M., Benson, B. A., Vikhlinin, A., et al. 2013, *ApJ*, 774, 23, doi: [10.1088/0004-637X/774/1/23](https://doi.org/10.1088/0004-637X/774/1/23)

McDonald, M., Stalder, B., Bayliss, M., et al. 2016a, *ApJ*, 817, 86, doi: [10.3847/0004-637X/817/2/86](https://doi.org/10.3847/0004-637X/817/2/86)

McDonald, M., Bulbul, E., de Haan, T., et al. 2016b, *ApJ*, 826, 124, doi: [10.3847/0004-637X/826/2/124](https://doi.org/10.3847/0004-637X/826/2/124)

McDonald, M., McNamara, B. R., Voit, G. M., et al. 2019, *ApJ*, 885, 63, doi: [10.3847/1538-4357/ab464c](https://doi.org/10.3847/1538-4357/ab464c)

McNamara, B. R., & Nulsen, P. E. J. 2007, *ARA&A*, 45, 117, doi: [10.1146/annurev.astro.45.051806.110625](https://doi.org/10.1146/annurev.astro.45.051806.110625)

—. 2012, *New Journal of Physics*, 14, 055023, doi: [10.1088/1367-2630/14/5/055023](https://doi.org/10.1088/1367-2630/14/5/055023)

Mernier, F., de Plaa, J., Kaastra, J. S., et al. 2017, *A&A*, 603, A80, doi: [10.1051/0004-6361/201630075](https://doi.org/10.1051/0004-6361/201630075)

NASA High Energy Astrophysics Science Archive Research Center (Heasarc). 2014, HEASoft: Unified Release of FTOOLS and XANADU, Astrophysics Source Code Library, record ascl:1408.004

Navarro, J. F., Frenk, C. S., & White, S. D. M. 1997, *ApJ*, 490, 493, doi: [10.1086/304888](https://doi.org/10.1086/304888)

O'Dea, C. P., Baum, S. A., Privon, G., et al. 2008, *ApJ*, 681, 1035, doi: [10.1086/588212](https://doi.org/10.1086/588212)

Panagoulia, E. K., Fabian, A. C., & Sanders, J. S. 2014, *MNRAS*, 438, 2341, doi: [10.1093/mnras/stt2349](https://doi.org/10.1093/mnras/stt2349)

Ponman, T. J., Cannon, D. B., & Navarro, J. F. 1999, *Nature*, 397, 135, doi: [10.1038/16410](https://doi.org/10.1038/16410)

Prasad, D., Sharma, P., Babul, A., Voit, G. M., & O'Shea, B. W. 2020, *MNRAS*, 495, 594, doi: [10.1093/mnras/staa1247](https://doi.org/10.1093/mnras/staa1247)

Pulido, F. A., McNamara, B. R., Edge, A. C., et al. 2018, *ApJ*, 853, 177, doi: [10.3847/1538-4357/aaa54b](https://doi.org/10.3847/1538-4357/aaa54b)

Rafferty, D. A., McNamara, B. R., Nulsen, P. E. J., & Wise, M. W. 2006, *ApJ*, 652, 216, doi: [10.1086/507672](https://doi.org/10.1086/507672)

Sabol, E. J., & Snowden, S. L. 2019, *sxrbg*: ROSAT X-Ray Background Tool, Astrophysics Source Code Library, record ascl:1904.001

Sarazin, C. L. 1986, *Reviews of Modern Physics*, 58, 1, doi: [10.1103/RevModPhys.58.1](https://doi.org/10.1103/RevModPhys.58.1)

Schlafly, E. F., & Finkbeiner, D. P. 2011, *ApJ*, 737, 103, doi: [10.1088/0004-637X/737/2/103](https://doi.org/10.1088/0004-637X/737/2/103)

Sharma, P., McCourt, M., Parrish, I. J., & Quataert, E. 2012, *MNRAS*, 427, 1219, doi: [10.1111/j.1365-2966.2012.22050.x](https://doi.org/10.1111/j.1365-2966.2012.22050.x)

Stueber, H. R., Mantz, A. B., Allen, S. W., et al. 2026, *ApJ*, 997, 320, doi: [10.3847/1538-4357/ae3005](https://doi.org/10.3847/1538-4357/ae3005)

Su, Y., Buote, D., Gastaldello, F., & Brighenti, F. 2015, *ApJ*, 805, 104, doi: [10.1088/0004-637X/805/2/104](https://doi.org/10.1088/0004-637X/805/2/104)

Sutherland, R. S., & Dopita, M. A. 1993, *ApJS*, 88, 253, doi: [10.1086/191823](https://doi.org/10.1086/191823)

Tchernin, C., Eckert, D., Ettori, S., et al. 2016, *A&A*, 595, A42, doi: [10.1051/0004-6361/201628183](https://doi.org/10.1051/0004-6361/201628183)

Urban, O., Werner, N., Allen, S. W., Simionescu, A., & Mantz, A. 2017, *MNRAS*, 470, 4583, doi: [10.1093/mnras/stx1542](https://doi.org/10.1093/mnras/stx1542)

Veronica, A., Reiprich, T. H., Pacaud, F., et al. 2025, arXiv e-prints, arXiv:2511.22319, doi: [10.48550/arXiv.2511.22319](https://doi.org/10.48550/arXiv.2511.22319)

Voit, G. M. 2005, *Reviews of Modern Physics*, 77, 207, doi: [10.1103/RevModPhys.77.207](https://doi.org/10.1103/RevModPhys.77.207)

Voit, G. M., Bryan, G. L., Balogh, M. L., & Bower, R. G. 2002, *ApJ*, 576, 601, doi: [10.1086/341864](https://doi.org/10.1086/341864)

Voit, G. M., Donahue, M., Bryan, G. L., & McDonald, M. 2015, *Nature*, 519, 203, doi: [10.1038/nature14167](https://doi.org/10.1038/nature14167)

Voit, G. M., Kay, S. T., & Bryan, G. L. 2005, *MNRAS*, 364, 909, doi: [10.1111/j.1365-2966.2005.09621.x](https://doi.org/10.1111/j.1365-2966.2005.09621.x)

Werner, N., Urban, O., Simionescu, A., & Allen, S. W. 2013, *Nature*, 502, 656, doi: [10.1038/nature12646](https://doi.org/10.1038/nature12646)

Werner, N., Oonk, J. B. R., Sun, M., et al. 2014, *MNRAS*, 439, 2291, doi: [10.1093/mnras/stu006](https://doi.org/10.1093/mnras/stu006)

White, D. A., Fabian, A. C., Forman, W., Jones, C., & Stern, C. 1991, *ApJ*, 375, 35, doi: [10.1086/170167](https://doi.org/10.1086/170167)

Williamson, R., Benson, B. A., High, F. W., et al. 2011, *ApJ*, 738, 139, doi: [10.1088/0004-637X/738/2/139](https://doi.org/10.1088/0004-637X/738/2/139)

Wise, M. W., Davis, J. E., Huenemoerder, D. P., Houck, J. C., & Dewey, D. 2013, MARX: Model of AXAF Response to X-rays, *Astrophysics Source Code Library*, record ascl:1302.001

Wright, E. L., Eisenhardt, P. R. M., Mainzer, A. K., et al. 2010, *AJ*, 140, 1868, doi: [10.1088/0004-6256/140/6/1868](https://doi.org/10.1088/0004-6256/140/6/1868)